Hindawi
Journal of Nanomaterials
Volume 2017, Article ID 5320989, 10 pages
https://doi.org/10.1155/2017/5320989

Research Article

Oxalic Acid-Assisted Hydrothermal Synthesis and Luminescent of Hexagonal $NaYF_4:Ln^{3+}$ (Ln = Sm, Eu, Yb/Er) Micro/Nanoplates

Feng Tao,[1,2] Zhishun Shen,[1] Zhijun Wang,[1,2] Da Shu,[1,3] Qi Liu,[1,2] and Yufeng Sun[1,2]

[1]*Department of Materials Science and Engineering, Anhui Polytechnic University, Wuhu, Anhui 241000, China*
[2]*Anhui Provincial Laboratory of High Performance Nonferrous Metals Material, Wuhu, Anhui 241000, China*
[3]*Key Laboratory of Advanced Manufacturing Technology, Ministry of Education, Guiyang, Guizhou 5500013, China*

Correspondence should be addressed to Zhijun Wang; zhijunwang@ahpu.edu.cn

Received 7 September 2016; Accepted 27 February 2017; Published 21 March 2017

Academic Editor: Jie Song

Hexagonal $NaYF_4:Ln^{3+}$ micro/nanoplates were successfully synthesized via a hydrothermal method using oxalic acid as a shape modifier. X-ray diffraction (XRD), field emission scanning electron microscopy (FE-SEM), transmission electron microscopy (TEM), and selected area electron diffraction (SAED) have been used to study the morphologies and crystal structure of the products. The effects of the pH values and the molar ratio of oxalic acid to NaOH on the crystal growth have been investigated in detail. The time-dependent experiments have been conducted to investigate the morphology evolution process, and based on the results, a possible growth mechanism was proposed. The photoluminescence properties of 5 mol% Eu^{3+} and 3 mol% Sm^{3+} doped $NaYF_4$ and 20 mol% Yb^{3+}/2 mol% Er^{3+} codoped $NaYF_4$ micro/nanoplates were investigated. The experimental results showed that $NaYF_4:Ln^{3+}$ micro/nanoplates have excellent luminescence and can be potential application in the field of light display systems, lasers, and optoelectronic devices.

1. Introduction

Two-dimensional (2D) nanostructures have attracted considerable attention in the past few years for their potential applications in information storage, lasers, transducer, light emitter, catalyst, and sensor [1–6]. As building blocks for constructing nanodevices, nanoplates or nanosheets are superior to spherical nanocrystals for their anisotropic structures, facile controlled crystal orientation synthetization, and large width-to-thickness aspect ratios [7]. Many monolayer materials with unique physical, electronic, and structural properties have emerged, such as layered transition metal chalcogenides (MoS_2, WS_2, $TiSe_2$, and Bi_2Se_3) [8, 9].

As an excellent host material for both down-conversion and up-conversion processes, $NaYF_4$ has attracted considerable attention due to its low lattice phonon energy and transparency in the visible and ultraviolet range, which could significantly reduce fluorescence quenching and expand its usability in flat-panel displays, optical storage, biolabels, solid-state lasers, and light-emitting diodes [10–17]. Furthermore, due to their low toxicity and good chemical stability, and unique dissolution-recrystallization growth process, $NaYF_4$ crystals are an ideal material for the research of crystal growth and propitious to both fundamental and practical research. Abundant efforts have been dedicated to controlled synthesis of $NaYF_4$ micro/nanocrystals with various morphologies [18–24]. Currently, much effort focused on the realization of 2D nano- and microstructures by controlling the sizes and shapes of rare earth fluorides [25–29], such as $NaLuF_4$ hexagonal microplates [25] and EuF_3 microdisks [26]. Recently, 2D $NaYF_4$ microcrystals have also been reported, Ding and coworkers [27] find that the molar ratio of NaF to Re^{3+} has a significant influence on the structures and shapes of the final products, and $NaYF_4$ microplates can be obtained at high NaF/Ln ratio. The effect of NaF on both the morphology and phase transition of $NaYF_4$ crystals has also been reported by Zhang and coworkers [28]. Zhao et al. have

studied the effect of NaOH on the morphologies of $NaYF_4$ nanodisk [29]. Wu et al. studied the effect of the different ligand on the crystal growth and phase transition processes of the $NaYF_4$ crystals and find that the regular hexagonal nanosheets can be obtained with increasing the ligand chain length [24].

Inorganic microcrystals with novel morphologies are of special significance in understanding the growth behavior and potential technological applications in microelectronic devices. Moreover, it is necessary to investigate the influence of different synthesis conditions on the crystal growth so as to reveal the growth mechanism and realize the controlled synthesis of $NaYF_4$ crystals [24]. In this paper, we report the synthesis of single crystal hexagonal β-$NaYF_4$:Ln^{3+} micro/nanoplates by the oxalic acid-assisted hydrothermal approach. The structure and formation processes were investigated in detail, and a possible mechanism of crystal growth has been preliminarily proposed based on the experimental results. Furthermore, the down-conversion (DC) emission for 5 mol% Eu^{3+} and 3 mol% Sm^{3+} doped $NaYF_4$ and up-conversion (UC) emission for 20 mol% Yb^{3+}/2 mol% Er^{3+} codoped $NaYF_4$ micro/nanoplates were investigated in detail. These results endow this kind of material with potential application in the field of light display systems, lasers, and optoelectronic devices.

2. Experimental Section

2.1. Chemicals. Yttrium oxide (Y_2O_3, 99.99%), ytterbium oxide (Yb_2O_3, 99.99%), erbium oxide (Er_2O_3, 99.99%), samarium oxide (Sm_2O_3, 99.99%), europium oxide (Eu_2O_3, 99.99%), oxalic acid ($H_2C_2O_4$, AR), sodium hydroxide (NaOH, AR), sodium fluoride (NaF, AR), and nitric acid (HNO_3, AR) were purchased from Shanghai Chemical Reagents Company. All reagents were of analytical grade and used without further purification. Deionized water was used throughout experiments.

2.2. Preparation. In a typical procedure, 1 mmol Y_2O_3 was dissolved in dilute HNO_3 (3 mol L^{-1}, 25 mL) completely to form a clear aqueous solution, and then, a mixed solution composed with 17.5 mmol NaOH and a certain amount of oxalic acid ($n_{\text{oxalic acid}}/n_{\text{NaOH}}$ = 0.3, 0.4, 0.5) were added to form the metal-oxalic complex. After magnetic stirring for 10 min, NaF (0.303 g, 7.22 mmol) was added to the mixture under vigorous stirring and the pH value was adjusted to the set value (3, 5, 6, 7, and 9) using a dilute NaOH solution. The resultant suspension was transferred into a 30 mL Teflon-lined autoclave. The Teflon vessel was then filled with distilled water up to about 80% of its volume. After the autoclave was tightly sealed, it was heated at 200°C for 1–24 h. Then, the autoclave was cooled to room temperature naturally. The products were collected by filtration and washed several times with distilled water and absolute ethanol in turn and then dried in air at 60°C for 12 h. Different hydrothermal treatment times at 200°C were select to investigate the morphological evolution process of $NaYF_4$ crystals. Additionally, $NaYF_4$:Ln^{3+} (5 mol% Eu^{3+}, 3 mol% Sm^{3+}, and 20% Yb^{3+}/2 mol% Er^{3+}) samples were prepared in a similar manner.

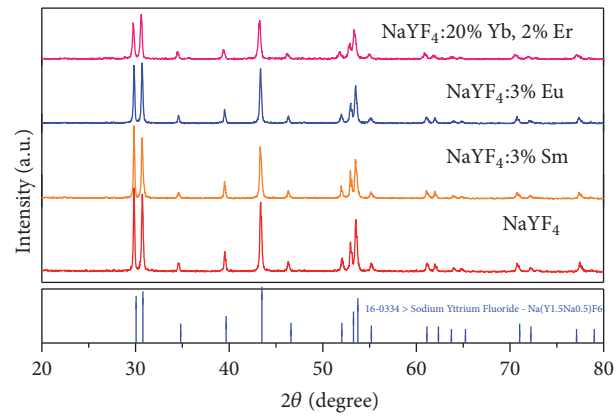

Figure 1: XRD patterns of the as-prepared β-$NaYF_4$ products at $n_{\text{oxalic acid}}/n_{\text{NaOH}}$ = 0.3 pH = 6, 200°C for 24 h.

2.3. Characterizations. X-ray diffraction (XRD) measurements were performed on an x-ray diffractometer (Rigaku, D/MAX-γ A) with Cu Kα radiation (λ = 0.15418 nm) in the range of $20^\circ \le 2\theta \le 80^\circ$. Scanning electron microscope (SEM) images were obtained on a field emission scanning electron microscope (FE-SEM, JSM-6700F). The high-resolution transmission electron microscope (HRTEM, JEOL 2010) and selected area electron diffraction (SAED) techniques were employed to characterize the crystal structure. Luminescence spectra were measured with a steady-state/lifetime fluorescence spectrometer (FLUOROLOG-3-TAU) at room temperature.

3. Results and Discussion

3.1. Morphology of the Products. Figure 1 shows the XRD patterns of the $NaYF_4$:Ln^{3+} product synthesized at pH = 6, $n_{\text{oxalic acid}}/n_{\text{NaOH}}$ = 0.3, 200°C for 24 h. As shown in Figure 1, the four samples exhibit the peaks of the pure hexagonal-phase $NaYF_4$, which are consistent with the literature data (JCPDS card number 16-0334). The peak intensity is different as the introduction of different dopant changed the $NaYF_4$ lattice parameters. No peaks of other impurity crystalline phases were detected, which indicates that the Ln^{3+} ions have been effectively doped into the host lattices. The high intensity of diffraction peaks further demonstrates the well-crystallized structure, which can be confirmed by the FE-SEM and HRTEM images.

The typical HRTEM and FE-SEM images for $NaYF_4$:Eu^{3+} sample are shown in Figure 2. Figure 2(a) shows that the product exhibits uniform micro/nanoplate with a perfect hexagonal shape and smooth surface, which indicates the high yield and high quality of the product obtained by this simple hydrothermal method. Figure 2(b) is the local magnified images of the samples; the analysis of a number of the products shows that these micro/nanoplates have an average edge length of 3.8 μm and a thickness of 90 nm. Figure 2(c)

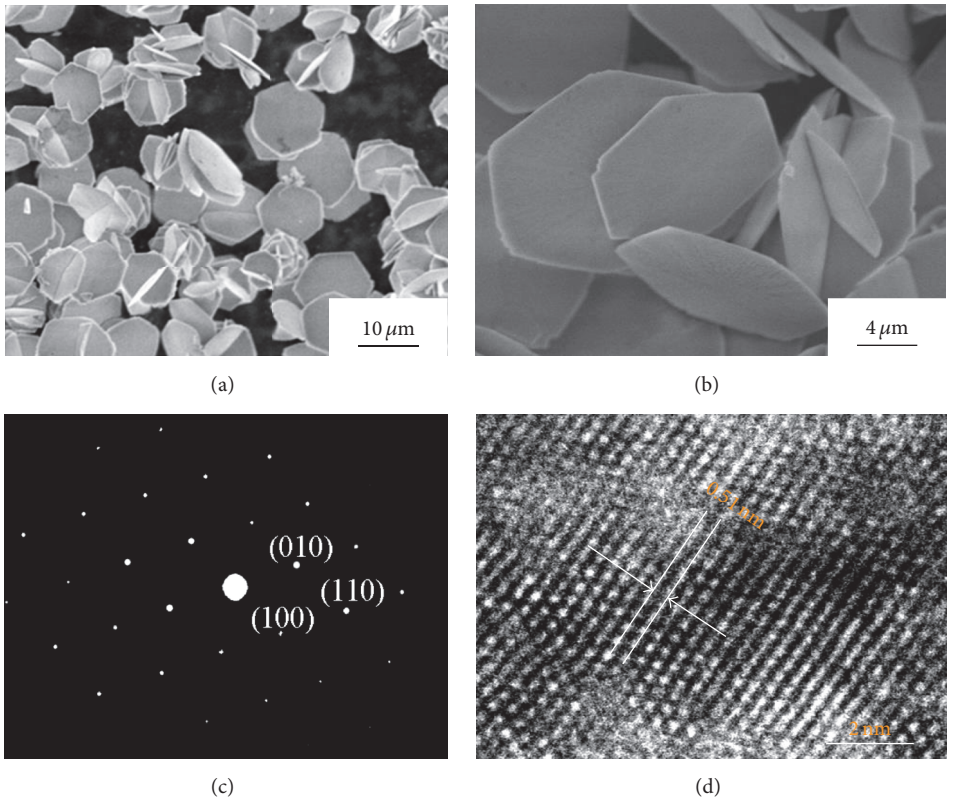

FIGURE 2: (a) Typical FE-SEM images of $NaYF_4$:Eu samples; (b) local magnified FE-SEM images; (c) SAED and (d) HRTEM of $NaYF_4$:Eu samples obtained at pH = 6, $n_{\text{oxalic acid}}/n_{\text{NaOH}}$ = 0.3, 200°C for 24 h.

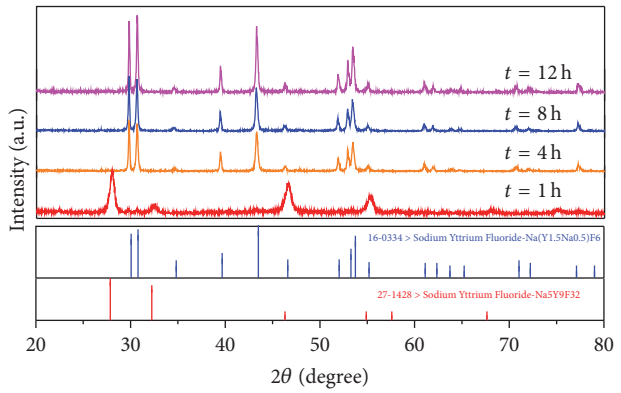

FIGURE 3: The XRD patterns of the $NaYF_4$:Yb^{3+}/Er^{3+} products after different times at pH = 6, 200°C.

shows the selected area electron diffraction (SAED) pattern. The diffraction spots are indexed to the (100), (010), and (110) planes of the hexagonal $NaYF_4$, which shows that the micro/nanoplate is a well-developed single crystal. HRTEM image in Figure 2(d) clearly shows the growth lattice fringes of the products. The measured lattice spacing is about 0.51 nm, corresponding to the distance of the {100} planes of the hexagonal $NaYF_4$. SAED and HRTEM results reveal the single crystal nature of the product.

3.2. Effect of Reaction Condition. To investigate the detailed formation mechanism of $NaYF_4$:Ln micro/nanoplates, time-dependent experiments were conducted while keeping the other reaction conditions unchanged. Figure 3 shows the XRD patterns of the products obtained at 200°C for different reaction time and standard data of α-$NaYF_4$ (JCPDS number 27-1428) and β-$NaYF_4$ (JCPDS number 16-0334) phases. It indicates that the samples display distinctively different XRD patterns at different reactions times. As shown in Figure 3, only cubic phase $NaYF_4$ can be obtained for 1 h. The phase transformation from cubic phase to hexagonal phase will take place in the following reaction. Pure hexagonal-phase $NaYF_4$ can be successfully obtained when the reaction time increased from 4 h to 12 h. The intensities of the diffraction

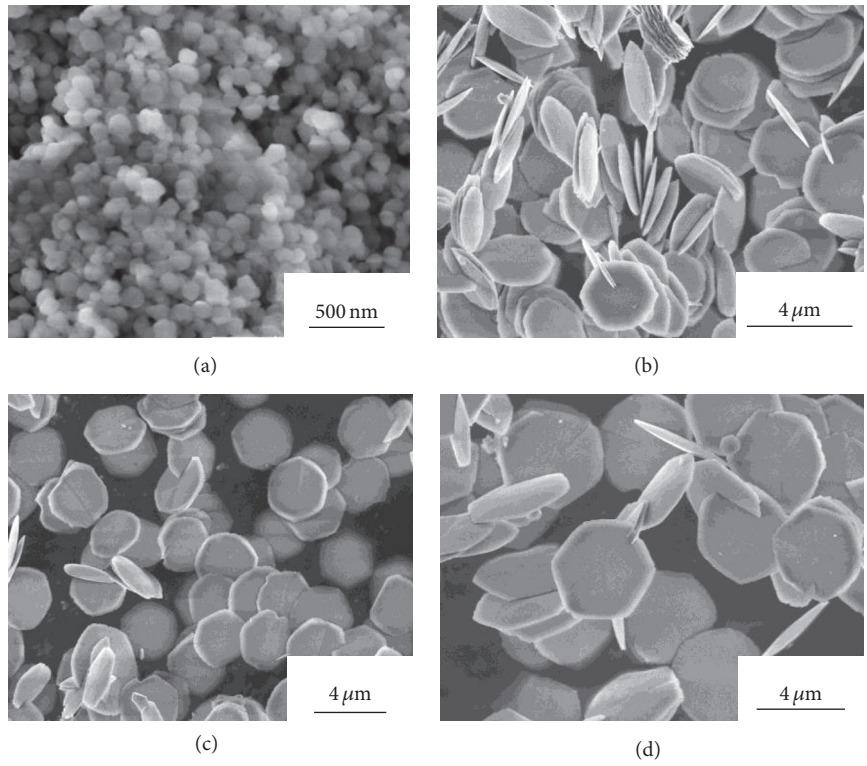

Figure 4: SEM images of the $NaYF_4$ products after different time at pH = 6, 200°C: (a) t = 1 h; (b) t = 4 h; (c) t = 8 h; (d) t = 12 h.

peaks increase significantly with increasing reaction time, which implied that the crystallinity of sample increases while the reaction proceeds.

Along with the phase transformation, the morphology of samples at different reaction time also changes. Figure 4 shows the SEM images of $NaYF_4$:Ln products with different reaction time. It is apparent that the four samples notably present different morphology during the crystal growth. When t = 1 h, spherical nanoparticles with a mean diameter of 80 nm are obtained clearly as shown in Figure 4(a), and when t = 4–12 h, micro/nanoplates are obtained (Figures 4(b)–4(d)). We can also find that when t = 4 h, the fairly uniform well-defined $NaYF_4$:Ln hexagonal micro/nanoplates with an average edge length of 1.8 μm and the thickness of 80 nm (Figure 4(b)) are obtained, while at t = 8 h and 12 h, the size of the products increases to 2 μm and 2.5 μm in edge length, respectively, but the borderline of the sheets is zigzag and not smooth. This indicated that the transversal and longitudinal growths happened with prolonged time. When t = 24 h, the size of the as-obtained products continues to augment significantly (3.2 μm in diameter and 90 nm in thickness) and the borderline is smooth as shown in Figure 2(b). According to the above process, the growth and directed attachment of the $NaYF_4$:Ln microparticles can be distinctly observed, which visually demonstrate the crystal growth and self-assembly process. It can be concluded that the cubic-hexagonal-phase transition directly results in the dramatic change in morphology of $NaYF_4$:Ln crystals. The change should be related to the different characteristic unit cell structures for different crystallographic phases. The cubic phase $NaYF_4$:Ln seeds have isotropic unit cell structures, which generally induce the isotropic growth of particles and therefore spherical particles are observed. However, hexagonal-phase $NaYF_4$:Ln seeds have anisotropic unit cell structures, which can induce anisotropic growth along crystallographic reactive directions, resulting in the formation of hexagonal structures [14, 16, 20, 21]. With prolonged reaction time, the morphology of the product is increasingly close to complete hexagon; it shows that the crystallization degree of the product is getting better and also consistent with the results of the XRD patterns.

A series of experiments were carried out to understand the formation mechanism of the $NaYF_4$:Ln micro/nanoplates. Figure 6 shows the FE-SEM images of the $NaYF_4$:Ln crystals prepared under different conditions, and the results indicated that the oxalic acid is indispensable to obtain the micro/nanoplates. As shown in Figure 6(a), if the oxalic acid was not added, the shape of the products is an incomplete hollow prism with 10 μm long, and the outer diameter of the tube-like prism is about 1 μm and inside diameter about 0.6 μm. The surfaces of these hollow prisms adhere many small particles. When $n_{\text{oxalic acid}}/n_{\text{NaOH}}$ = 0.3, as shown in Figure 6(b) the shape of the products is hexagonal microsheets with the edge length of 2 μm and 120 nm in thickness. When $n_{\text{oxalic acid}}/n_{\text{NaOH}}$ is increased to 0.4, there is no significant change in the morphology as shown in Figure 6(c), but the edge length increased to 3.2 μm and thickness was 150 nm. From Figure 6(c), we also can find that parts of the sheets are stacked and interspersed with each other, and the dispersion is bad. However, when

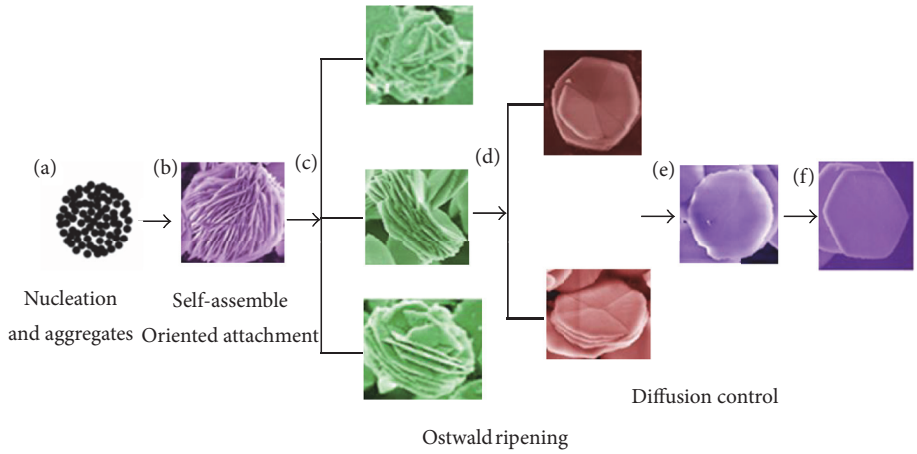

FIGURE 5: Schematic diagrams for the growth process based on the time-dependent experiments: (a) 1 h; (b) 4 h; (c) 8 h; (d-e) 12 h; and (f) 24 h.

$n_{\text{oxalic acid}}/n_{\text{NaOH}}$ was increased to 0.5, the morphology of the products has greatly changed from micro/nanosheet to quadrate with the length of 14.1 μm and thickness of 2.3 μm (Figure 6(d)).

In our system, the oxalic acid is the chelating agent. At the early stage, the oxalic acid introduced to the reaction system can form complexes with RE^{3+} ions through strong coordination interaction. But the chelating ability of the RE^{3+}-$C_2O_4^{2-}$ complexes will be affected by the local environment such as pH value. A suitable pH value can kinetically control the growth rate of micro/nanoplates. Figure 7 gives the FE-SEM images of the products obtained under different pH value. When the pH value is 3 (Figure 7(a)), the product is a 3D structure stacked together by 3–5 round sheets and the diameter is about 1.7 μm. It is also noticed that each micro/nanoplate is composed of several small slices with a thickness of approximately 50 nm. However, when the pH value is increased to 5, the morphology of the product is the uniformity, round disks with smooth surfaces (Figure 7(b)), and the average diameter is 2.4 μm and the center thickness is 0.23 μm. When the pH value is up to 7, the product is regular hexagonal micro/nanoplates with 0.18 μm thicknesses and 1.1 μm edge length as shown in Figure 7(c). Further increasing the pH value to 9, the microspheres can be observed, and the average diameter is 5 μm as shown in Figure 7(d). Inset is the local magnified image of a single microsphere, which indicates that the microsphere is constituted by many long strips crystals. The above results show that different pH value affects the growth and orientation of the crystals, and so the morphologies of the products have great changes. In this experiment, oxalic acid was used as a chelating agent. The pH value has a significant effect on the selective adsorption of oxalate acid ion onto the different surfaces of growing $NaYF_4$:Ln crystallites and then gives rise to the difference in the growth rates between different crystallographic directions [29].

In the present work, based on the time-dependent experiments, the schematic illustration of the possible growth process is shown in Figure 5. When reaching the critical supersaturation of the particle-forming species, $NaYF_4$:Ln nuclei will be generated by the reaction among Na^+, F^-, and RE^{3+}. In a very short reaction time, these nuclei can only grow into cubic-phased $NaYF_4$:Ln irregular nanoparticles (Figure 5(a)). The cubic $NaYF_4$:Ln seeds have isotropic unit cell structures, inducing an isotropic growth of particle. Therefore, spherical particles are observed in order to minimize the surface energy of the crystal facets. However, these cubic-phased $NaYF_4$:Ln particles are unstable and phase transition takes place to form stable hexagonal-phased $NaYF_4$:Ln particle when the reaction time increased to more than 4 h. During the following reaction process, accompanying with the phase transition, oriented attachment will occur among those adjacent nanoparticles to form two-dimensional sheets along the space structure, which eventually forms the complex flower-like microstructures (Figure 5(b)) [26], so we can find a little flower-like complex structure piled up with microsheet in Figures 2 and 4. With the reaction process continuing, Ostwald ripening process will happen among those sheets (Figure 5(c)) and the diffusion-control growth will occur on their surface (Figure 5(d)) by adsorbing the nutrient elements from the surrounding solution, and then relatively simple sheets will be formed as a result of the different growth rates of different crystal faces as shown in Figure 5(e and f) and the eventual morphology is the regular hexagon.

4. Photoluminescence Properties

It has been reported that the 2D nanostructures have higher luminous intensity than the other shapes nanocrystals. Yin et al. have reported that the 2D MoS_2 nanosheets have higher luminous intensity than the other shapes MoS_2 nanocrystals [30]. Yang et al. reported the synthesis of uniform hexagonal LaF_3:Eu^{3+} nanoplates by the aid of glycine as the complexing and capping agent under the hydrothermal methods. The relative intensities of the emission peaks in nanoplates are obviously stronger than those of the irregular nanoparticles and nonuniform nanoplates [31]. It is well known that the hexagonal $NaYF_4$ is a much better host lattice for the luminescence of various optical lanthanide ions.

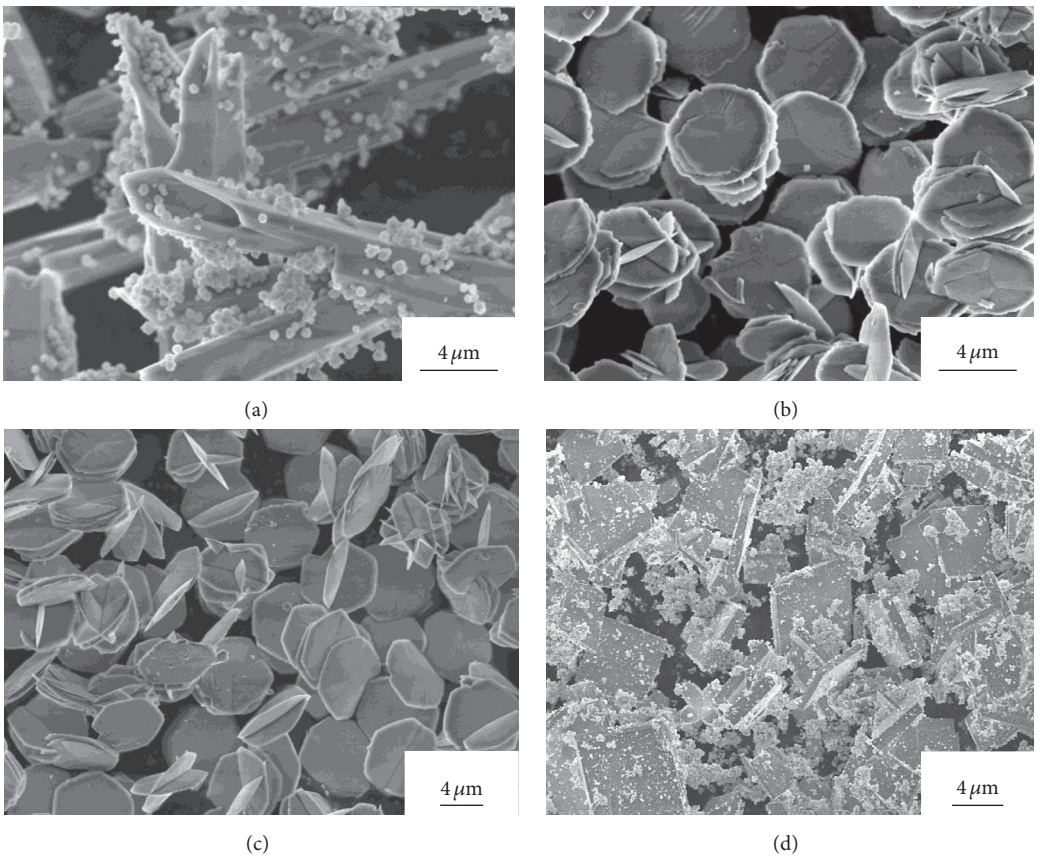

FIGURE 6: SEM image of $NaYF_4$ product with different concentration of chelating agent, 200°C, 12 h, $n(Y^{3+}) : n(F^-) = 1 : 6.5$, pH = 6, $n_{\text{oxalic acid}}/n_{\text{NaOH}}$ = (a) 0; (b) 0.3; (c) 0.4; (d) 0.5.

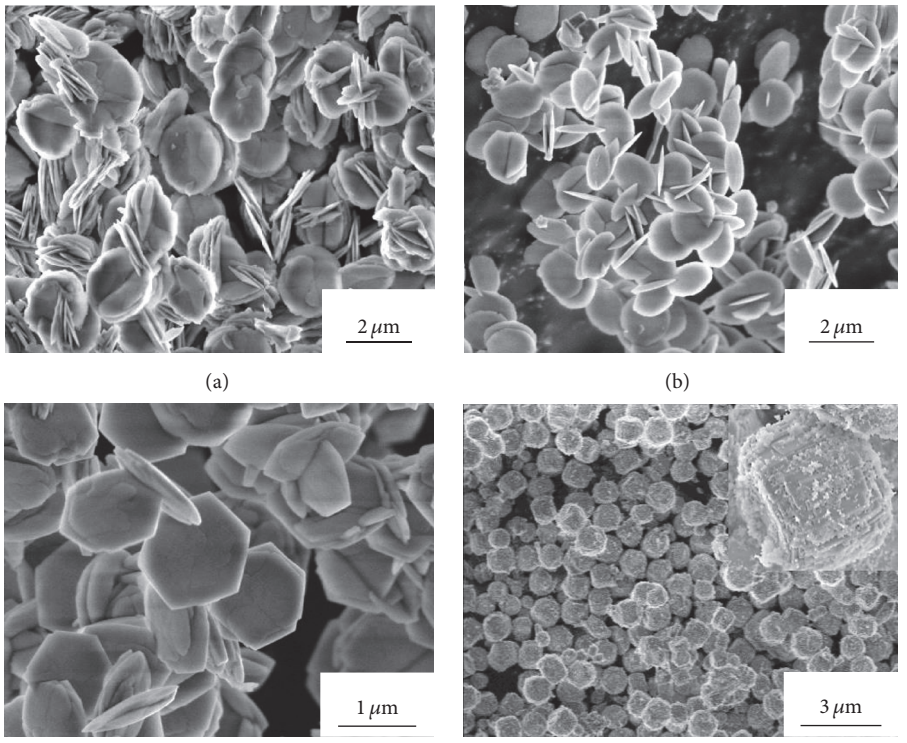

FIGURE 7: SEM images of the $NaYF_4$ products at different pH value (24 h, 200°C): (a) pH = 3; (b) pH = 5; (c) pH = 7; and (d) pH = 9; insert is the local magnified image of a single microsphere.

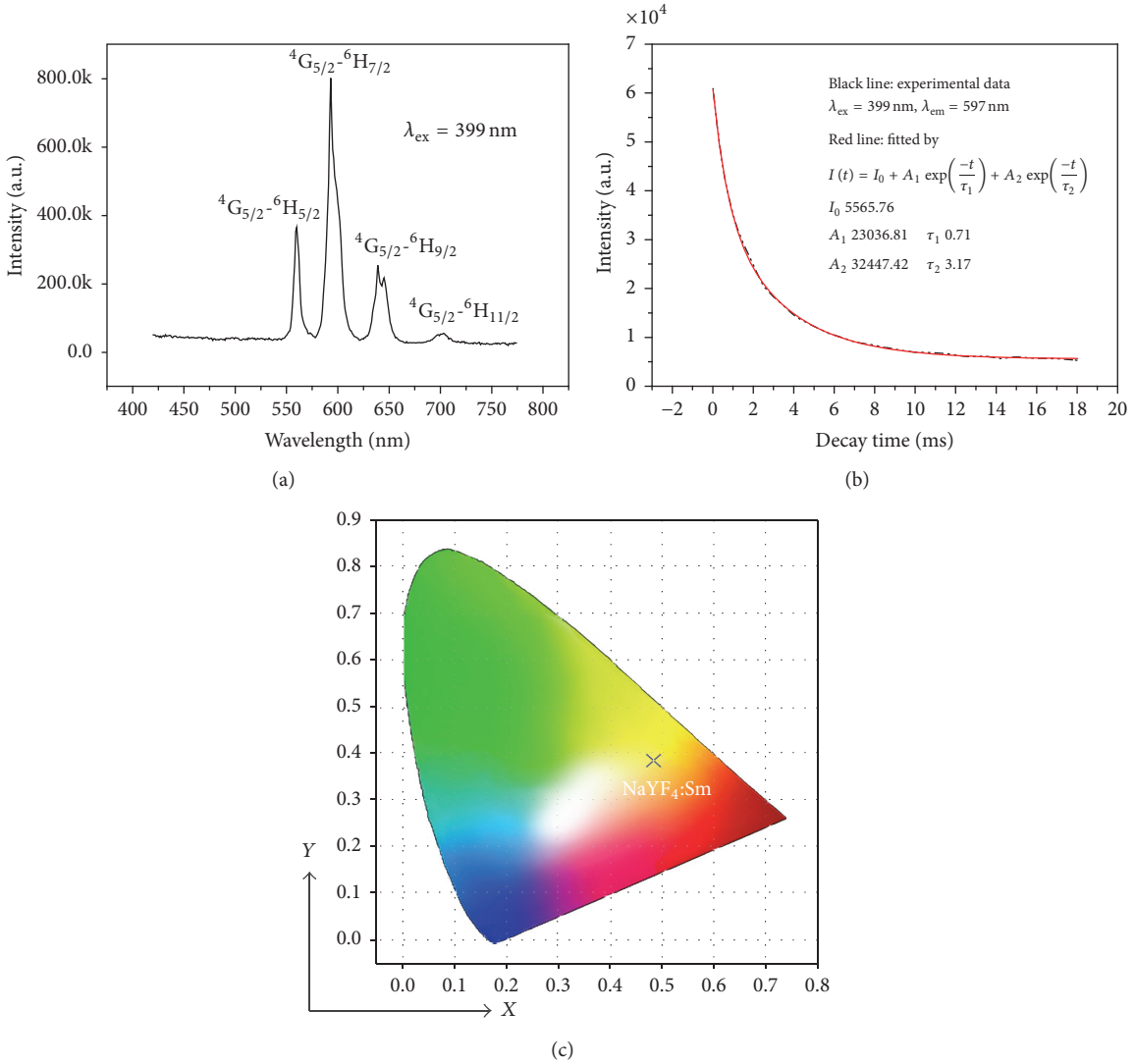

FIGURE 8: (a) Room temperature emission spectrum (Ex slits = 2 nm, Em slits = 5 nm), (b) the decay curve of Sm^{3+} ($^4D_{4/2}$-$^6H_{7/2}$), and (c) the CIE chromaticity diagram for the $NaYF_4$:3% Sm^{3+} samples.

Here we also investigate the PL properties of the as-formed $NaYF_4$:Ln^{3+} hexagonal micro/nanosheets. To investigate the luminescence properties, Eu^{3+}, Sm^{3+}, and Yb^{3+}/Er^{3+} are selected as doped ion [16, 17]. Figure 8(a) displays the room temperature emission (λ_{ex} = 399 nm) spectra of 3 mol% Sm^{3+} doped $NaYF_4$ micro/nanoplates. Three strong emission bands are observed at ~559, ~593, and ~639 nm in the yellow to red region, which corresponds to a group of typical $^4G_{5/2}$-^6H_J (J = 5/2, 7/2, 9/2) transitions of Sm^{3+} and one weak emission band at 703 nm for the transition of $^4G_{5/2}$-$^6H_{11/2}$ for Sm^{3+}. Figure 8(b) shows the luminescence decay curve of the 593 nm emission when Sm^{3+} was excited directly at 399 nm. The decay curve can be fitted well with a double exponential function as $I(t) = I_0 + A_0 \exp(-t/\tau_1) + A_1 \exp(-t/\tau_2)$ (I_0 is the initial emission intensity at $t = 0$ and τ is the 1/e life time of the emission center, $\tau = (A_1\tau_1^2 + A_2\tau_2^2)/(A_1\tau_1 + A_2\tau_2)$). The lifetime for $^4G_{5/2}$-$^6H_{7/2}$ of Sm^{3+} is 2.83 ms. Figure 8(c) shows the CIE chromaticity diagram for 3 mol% Sm doped $NaYF_4$ micro/nanoplates under 399 nm excitation wavelength. $NaYF_4$:Sm micro/nanoplates exhibit yellow color (CIE chromaticity coordinates x = 0.478, y = 0.390).

The same procedure was used to study doped $NaYF_4$ microstructures with Eu^{3+}, Yb^{3+}/Er^{3+}. Figure 9 shows the room temperature emission (excited at 393 nm) spectra of the $NaYF_4$:Eu^{3+} (5%) micro/nanoplates suspended in absolute ethanol. It consists of the emission lines mainly in the red spectrum range from 575 to 630 nm associated with the Eu^{3+} transitions from the excited $^5D_0$ and $^5D_1$ levels to the ^7F_j (j = 1, 2, 3, 4) levels. The most intense peaks are centered at 614 nm. There is no notable shift in positions of the emission peaks compared to other Eu^{3+}-doped systems since the 4f energy levels of Eu^{3+} are hardly affected by the crystal field because of the shielding effect of the $5s^25p^6$ electrons. Figure 9(b) shows the luminescence decay curve of the 614 nm emission

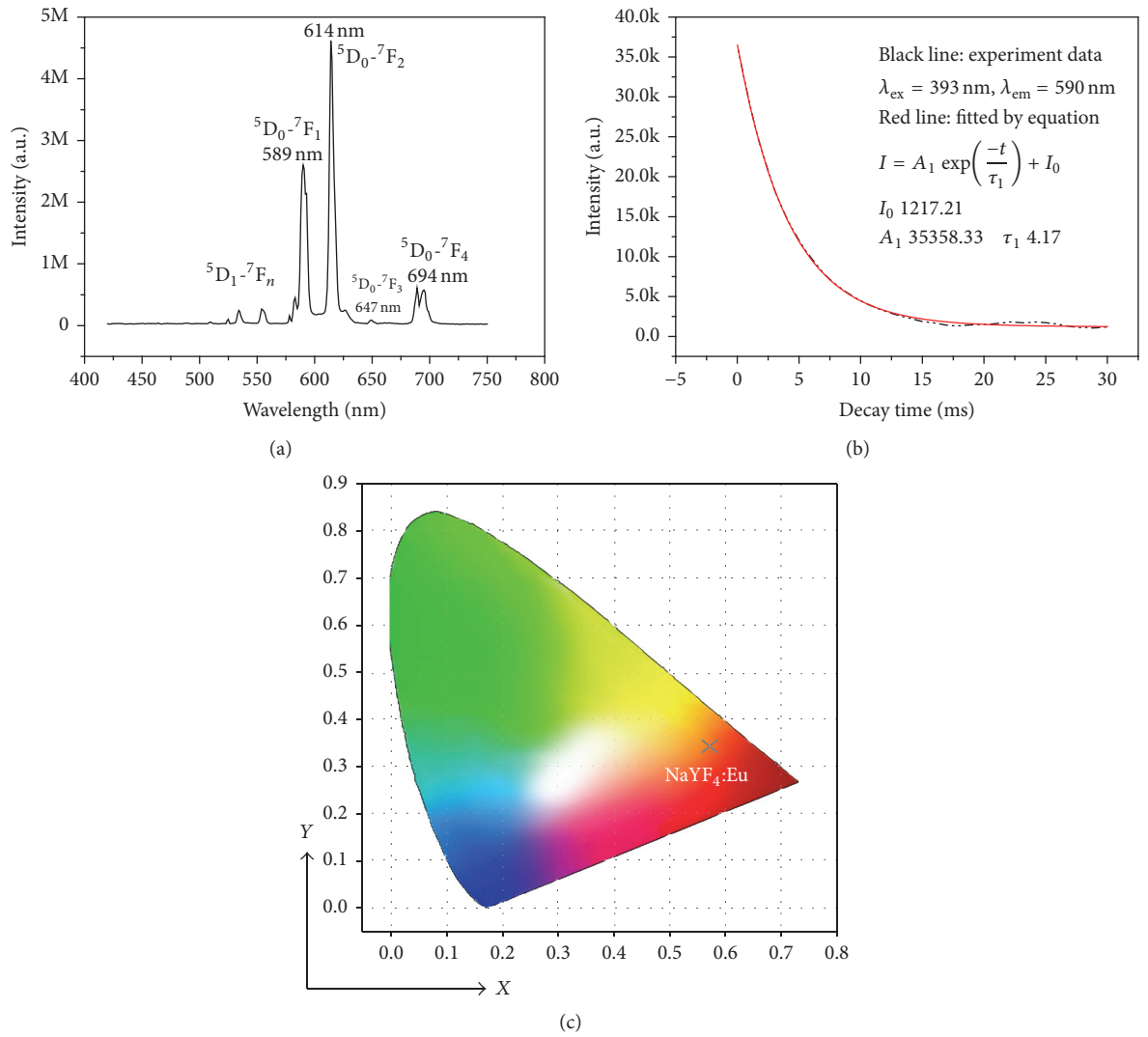

FIGURE 9: (a) Room temperature emission spectrum (Ex slits = 2 nm, Em slits = 5 nm), (b) the decay curve of Eu^{3+} ($^5D_0$-$^7F_2$), and (c) the CIE chromaticity diagram for the $NaYF_4$:5% Eu^{3+} samples.

when Eu^{3+} was excited directly at 393 nm. The decay curve can be fitted well with a single exponential function as $I(t) = A_1 \exp(-t/\tau) + I_0$. The luminescence lifetime for $^5D_0$-$^7F_2$ of Eu^{3+} is determined to be 4.17 ms. Figure 9(c) shows the CIE chromaticity diagram for 3 mol% Eu doped $NaYF_4$ microcrystal under 323 nm excitation wavelength. $NaYF_4$:Eu micro/nanoplates exhibit orange-red color (CIE chromaticity coordinates $x = 0.583$, $y = 0.379$).

Figure 10 shows the room emission spectra of as-synthesized micro/nanoplates (as shown in Figure 2(b)) samples under infrared excitation (980 nm laser). The results show obvious green emission peaks centered at 521 nm ($^2H_{11/2} \rightarrow {}^4I_{15/2}$) and 540 nm ($^4S_{3/2} \rightarrow {}^4I_{15/2}$), a red emission peak centered at 654 nm ($^4F_{9/2} \rightarrow {}^4I_{15/2}$), and one weak blue emission peak centered at 408 nm ($^2H_{9/2} \rightarrow {}^4I_{15/2}$), associated with transitions of Er^{3+} ions similar to that for $NaYF_4$:Yb^{3+}/Er^{3+} nanocrystals and bulks reported previously [32, 33]. The observation of 408 nm emissions provides another direct evidence for the high UC efficiency of this sample [27, 33]. Among those emissions peaks, the green emission (521 and 540 nm) intensity is stronger than that of the red emission (654 nm) and relative intensity ratio of green (500–570) to red (630–680) emission ($R_{G/R}$) is 2.58, which shows that the electron transition via an energy-transfer up-conversion (ETU) process is much higher than that via a nonradiative relaxation. Figure 10(b) shows the CIE chromaticity diagram for 20 mol% Yb^{3+}/2 mol% Er^{3+} codoped $NaYF_4$ microcrystal under the excitation wavelength of 980 nm. $NaYF_4$:Yb, Er micro/nanoplates exhibit green (CIE chromaticity coordinates $x = 0.263$, $y = 0.694$).

5. Conclusions

In summary, hexagonal $NaYF_4$:Ln^{3+} (Ln = Sm, Eu, Yb/Er) micro/nanoplates were successfully synthesized via an oxalic

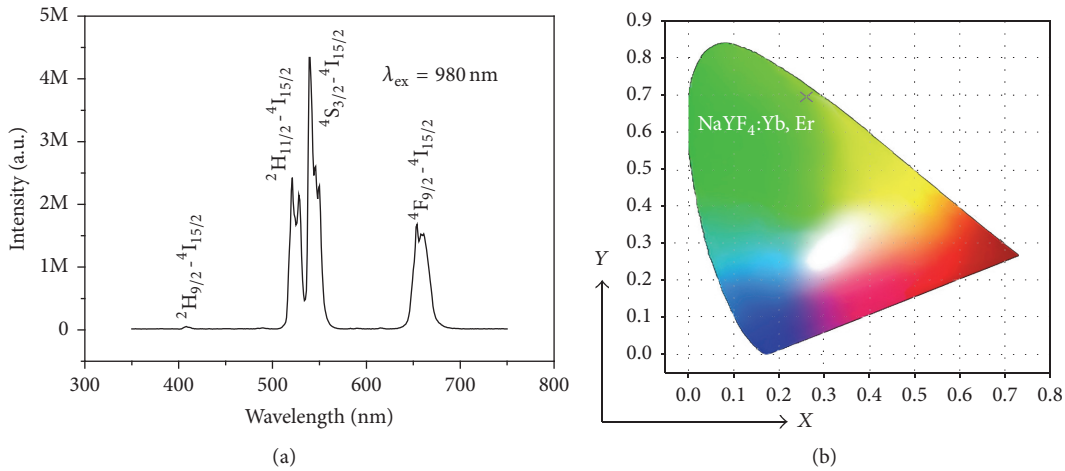

FIGURE 10: (a) Room temperature UC emission spectrum (Ex slits = 2 nm, Em slits = 5 nm) and (b) the CIE chromaticity diagram for the $NaYF_4$:Yb^{3+}/Er^{3+} samples.

acid-assisted hydrothermal method. XRD and FE-SEM results show that pure hexagonal-phase $NaYF_4$ products were obtained. The HRTEM images and SAED show the single crystal nature of the micro/nanoplates. The formation mechanism of micro/nanoplates has been investigated in detail. The inherent growth habit and the specific interaction between oxalic acid and the different crystal surface play important roles in the formation process of the final products. The investigation on the Sm^{3+} and Eu^{3+} doped hexagonal $NaYF_4$ micro/nanoplates DC spectra and Yb^{3+}/Er^{3+} codoped hexagonal $NaYF_4$ micro/nanoplates UC spectrum indicates that $NaYF_4$:Ln^{3+} micro/nanoplates are also an excellent luminescence material and can be potential application in the field of light display systems, lasers, and optoelectronic devices. This study is also expected to provide important information for morphology controlled synthesis of other complex rare earth fluoride compounds.

Conflicts of Interest

The authors declare that they have no conflicts of interest.

Acknowledgments

This work was supported by National Natural Science Foundation of China (Grants nos. 61174012 and 51302001), Anhui Natural Science Foundation (Grant no. 1408085ME92), Foundation for Excellent Talents in University by Anhui Province (Grant no. 2012SQRL082ZD), the Natural Science Research Project of Anhui Provincial Universities Funded by the Anhui Education Department (Grant no. KJ2013A038), and the Open Fund of Key Laboratory of Advanced Manufacturing Technology, Ministry of Education (Grant no. XDSYS2016001).

References

[1] J. N. Coleman, M. Lotya, A. O'Neill et al., "Two-dimensional nanosheets produced by liquid exfoliation of layered materials," *Science*, vol. 331, pp. 568–571, 2011.

[2] Y. Wang, C. Sun, X. Yan et al., "Lattice distortion oriented angular self-assembly of monolayer titania sheets," *Journal of the American Chemical Society*, vol. 133, no. 4, pp. 695–697, 2011.

[3] B. Radisavljevic, A. Radenovic, J. Brivio, V. Giacometti, and A. Kis, "Single-layer MoS_2 transistors," *Nature Nanotechnology*, vol. 6, no. 3, pp. 147–150, 2011.

[4] Z. Y. Tang, Z. L. Zhang, Y. Wang, S. C. Glotzer, and N. A. Kotov, "Self-assembly of CdTe nanocrystals into free-floating sheets," *Science*, vol. 314, no. 5797, pp. 274–278, 2006.

[5] Y. Sun, Z. Sun, S. Gao et al., "Fabrication of flexible and freestanding zinc chalcogenide single layers," *Nature Communications*, vol. 3, 2012.

[6] Y. Du, Z. Yin, J. Zhu et al., "A general method for the large-scale synthesis of uniform ultrathin metal sulphide nanocrystals," *Nature Communications*, vol. 3, article no. 1177, 2012.

[7] C. Schliehe, B. H. Juarez, M. Pelletier et al., "Ultrathin PbS sheets by two-dimensional oriented attachment," *Science*, vol. 329, no. 5991, pp. 550–553, 2010.

[8] K. J. Koski and Y. Cui, "The new skinny in two-dimensional nanomaterials," *ACS Nano*, vol. 7, no. 5, pp. 3739–3743, 2013.

[9] K. F. Mak, C. Lee, J. Hone, J. Shan, and T. F. Heinz, "Atomically thin MoS_2: a new direct-gap semiconductor," *Physical Review Letters*, vol. 105, no. 13, Article ID 136805, 2010.

[10] J. Zhou, Z. Liu, and F. Li, "Upconversion nanophosphors for small-animal imaging," *Chemical Society Reviews*, vol. 41, no. 3, pp. 1323–1349, 2012.

[11] Y. Wei, X. Li, and H. Guo, "Enhanced upconversion in novel KLu_2F_7: Er^{3+} transparent oxyfluoride glass-ceramics," *Optical Materials Express*, vol. 4, no. 7, pp. 1367–1372, 2014.

[12] F. Wang, Y. Han, C. S. Lim et al., "Simultaneous phase and size control of upconversion nanocrystals through lanthanide doping," *Nature*, vol. 463, no. 7284, pp. 1061–1065, 2010.

[13] R. Deng, F. Qin, R. Chen, W. Huang, M. Hong, and X. Liu, "Temporal full-colour tuning through non-steady-state upconversion," *Nature Nanotechnology*, vol. 10, no. 3, pp. 237–242, 2015.

[14] M. Ding, S. Yin, D. Chen et al., "Hexagonal $NaYF_4$:Yb^{3+}/Er^{3+} nano/micro-structures: controlled hydrothermal synthesis and morphology-dependent upconversion luminescence," *Applied Surface Science*, vol. 333, pp. 23–33, 2015.

[15] M. Lin, Y. Zhao, M. Liu et al., "Synthesis of upconversion $NaYF_4$:Yb^{3+},Er^{3+} particles with enhanced luminescent intensity through control of morphology and phase," *Journal of Materials Chemistry C*, vol. 2, no. 19, pp. 3671–3676, 2014.

[16] X. Wang, J. Zhuang, Q. Peng, and Y. Li, "Hydrothermal synthesis of rare-earth fluoride nanocrystals," *Inorganic Chemistry*, vol. 45, no. 17, pp. 6661–6665, 2006.

[17] H.-S. Qian and Y. Zhang, "Synthesis of hexagonal-phase core-shell $NaYF_4$ nanocrystals with tunable upconversion fluorescence," *Langmuir*, vol. 24, no. 21, pp. 12123–12125, 2008.

[18] M. Y. Ding, C. H. Lu, L. H. Cao, J. B. Song, Y. R. Ni, and Z. Z. Xu, "Facile synthesis of β-$NaYF_4$:Ln^{3+} (Ln = Eu, Tb, Yb/Er, Yb/Tm) microcrystals with down- and up-conversion luminescence," *Journal of Material Science*, vol. 48, no. 14, pp. 4989–4998, 2013.

[19] M. Ding, C. Lu, Y. Song, Y. Ni, and Z. Xu, "Hydrothermal synthesis of ordered β-$NaYF_4$ nanorod self-assemblies with multicolor up- and down-conversions," *CrystEngComm*, vol. 16, no. 6, pp. 1163–1173, 2014.

[20] D.-K. Ma, S.-M. Huang, Y.-Y. Yu, Y.-F. Xu, and Y.-Q. Dong, "Rare-earth-ion-doped hexagonal-phase $NaYF_4$ nanowires: controlled synthesis and luminescent properties," *Journal of Physical Chemistry C*, vol. 113, no. 19, pp. 8136–8142, 2009.

[21] X. Liang, X. Wang, J. Zhuang, Q. Peng, and Y. Li, "Branched $NaYF_4$ nanocrystals with luminescent properties," *Inorganic Chemistry*, vol. 46, no. 15, pp. 6050–6055, 2007.

[22] H.-X. Mai, Y.-W. Zhang, L.-D. Sun, and C.-H. Yan, "Highly efficient multicolor up-conversion emissions and their mechanisms of monodisperse NaYF4:Yb,Er core and core/shell-structured nanocrystals," *Journal of Physical Chemistry C*, vol. 111, no. 37, pp. 13721–13729, 2007.

[23] Y. Wei, F. Lu, X. Zhang, and D. Chen, "Synthesis of oil-dispersible hexagonal-phase and hexagonal-shaped $NaYF_4$:Yb, Er nanoplates," *Chemistry of Materials*, vol. 18, no. 24, pp. 5733–5737, 2006.

[24] S. Wu, Y. Liu, J. Chang, and S. Zhang, "Ligand dynamic effect on phase and morphology control of hexagonal $NaYF_4$," *CrystEngComm*, vol. 16, no. 21, pp. 4472–4477, 2014.

[25] C. Li, J. Yang, P. Yang, X. Zhang, H. Lian, and J. Lin, "Two-dimensional β-$NaLuF_4$ hexagonal microplates," *Crystal Growth and Design*, vol. 8, no. 3, pp. 923–929, 2008.

[26] Z. Chen, Z. Geng, D. Shao, Y. Mei, and Z. Wang, "Single-crystalline EuF_3 hollow hexagonal microdisks: synthesis and application as a background-free matrix for MALDI-TOF-MS analysis of small molecules and polyethylene glycols," *Analytical Chemistry*, vol. 81, no. 18, pp. 7625–7631, 2009.

[27] M. Ding, C. Lu, L. Cao, Y. Ni, and Z. Xu, "Controllable synthesis, formation mechanism and upconversion luminescence of β-$NaYF_4$:Yb^{3+}/Er^{3+} microcrystals by hydrothermal process," *CrystEngComm*, vol. 15, no. 41, pp. 8366–8373, 2013.

[28] F. Zhang, J. Li, J. Shan, L. Xu, and D. Zhao, "Shape, size, and phase-controlled rare-earth fluoride nanocrystals with optical up-conversion properties," *Chemistry—A European Journal*, vol. 15, no. 41, pp. 11010–11019, 2009.

[29] J. Zhao, Y. Sun, X. Kong et al., "Controlled synthesis, formation mechanism, and great enhancement of red upconversion luminescence of $NaYF_4$:Yb^{3+}, Er^{3+} nanocrystals/submicroplates at low doping level," *The Journal of Physical Chemistry B*, vol. 112, no. 49, pp. 15666–15672, 2008.

[30] Z. Yin, H. Li, H. Li et al., "Single-layer MoS_2 phototransistors," *ACS Nano*, vol. 6, no. 1, pp. 74–80, 2012.

[31] X. Yang, X. Dong, J. Wang, and G. Liu, "Glycine-assisted hydrothermal synthesis of single-crystalline LaF_3:Eu^{3+} hexagonal nanoplates," *Journal of Alloys and Compounds*, vol. 487, no. 1-2, pp. 298–303, 2009.

[32] S. Som, M. Chowdhury, and S. K. Sharma, "Band gap and trapping parameters of color tunable Yb^{3+}/Er^{3+} codoped Y_2O_3 upconversion phosphor synthesized by combustion route," *Journal of Materials Science*, vol. 49, no. 2, pp. 858–867, 2014.

[33] F. Wang, J. Wang, and X. Liu, "Direct evidence of a surface quenching effect on size-dependent luminescence of upconversion nanoparticles," *Angewandte Chemie—International Edition*, vol. 49, no. 41, pp. 7456–7460, 2010.